Enhancement of lanthanide evaporation by complexation: Dysprosium tri-iodide mixed with indium iodide and thulium tri-iodide mixed with thallium iodide

J. J. Curry, E. G. Estupiñán, A. Henins, W. P. Lapatovich, S. D. Shastri et al.

Citation: J. Chem. Phys. **139**, 124310 (2013); doi: 10.1063/1.4821828
View online: http://dx.doi.org/10.1063/1.4821828
View Table of Contents: http://jcp.aip.org/resource/1/JCPSA6/v139/i12
Published by the AIP Publishing LLC.

Enhancement of lanthanide evaporation by complexation: Dysprosium tri-iodide mixed with indium iodide and thulium tri-iodide mixed with thallium iodide

J. J. Curry,[1,a)] E. G. Estupiñán,[2] A. Henins,[1] W. P. Lapatovich,[3] S. D. Shastri,[4] and J. E. Hardis[1]

[1]*National Institute of Standards and Technology, 100 Bureau Drive, Gaithersburg, Maryland 20899, USA*
[2]*OSRAM SYLVANIA Inc., 71 Cherry Hill Drive, Beverly, Massachusetts 01915, USA*
[3]*Walter Lapatovich Consulting, 51 Pye Brook Lane, Boxford, Massachusetts 01921, USA*
[4]*Advanced Photon Source, Argonne National Laboratory, 9700 South Cass Avenue, Argonne, Illinois 60439, USA*

(Received 9 May 2013; accepted 6 September 2013; published online 30 September 2013)

The vapors in equilibrium with condensates of DyI_3, DyI_3/InI, TmI_3, and TmI_3/TlI were observed over the temperature range from 900 K to 1400 K using x-ray induced fluorescence. The total densities of each element (Dy, Tm, In, Tl, and I) in the vapor, summed over all atomic and molecular species, were determined. Dramatic enhancements in the total vapor densities of Dy and Tm were observed in the vapors over DyI_3/InI and TmI_3/TlI as compared to the vapors over pure DyI_3 and pure TmI_3, respectively. An enhancement factor exceeding 10 was observed for Dy at $T \approx 1020$ K, decreasing to 0 at $T \approx 1250$ K. An enhancement factor exceeding 20 was observed for Tm at $T \approx 1040$ K, decreasing to 0 at $T \approx 1300$ K. Such enhancements are expected from the formation of the vapor-phase hetero-complexes $DyInI_4$ and $TmTlI_4$. Numerical simulations of the thermochemical equilibrium suggest the importance of additional complexes in liquid phases. A description of the measurement technique is given. Improvements in the absolute calibration lead to an approximately 40% correction to previously reported preliminary results [J. J. Curry *et al.*, Chem. Phys. Lett. **507**, 52 (2011); Appl. Phys. Lett. **100**, 083505 (2012)]. © *2013 AIP Publishing LLC*. [http://dx.doi.org/10.1063/1.4821828]

I. INTRODUCTION

Metal-halide high-intensity discharge (MH-HID) lamps achieve high luminous efficacy and excellent color-rendering by utilizing the rich visible emission that can be obtained from the atoms and singly charged ions of a number of metals, including several lanthanide metals.[1] Such metals, which generally have very low vapor pressures, are introduced into lamps in the form of metal-halide salts, primarily metal-iodides. The heat of the lamp discharge is sufficient to raise the coldest regions of the discharge vessel, where salt condensates eventually accumulate, to over 1000 K. These cold-spot temperatures produce metal-halide vapor pressures in the range of 1 Pa–10^4 Pa. In hotter regions of the discharge vessel, the metal-halide molecules dissociate to varying degrees; in the core of the discharge, where temperatures routinely reach and may exceed 5000 K, molecules are completely dissociated into their constituent atoms. Core temperatures are high enough to cause significant excitation and ionization of the metal atoms. The metals used in HID lamps are chosen because of the low temperatures at which they are excited and ionized, and the copious visible radiation they subsequently emit.

The densities of radiating atoms in the core of a MH-HID lamp depend on many interacting phenomena, including non-equilibrium fluid transport. Although the core densities may not be in equilibrium with the relatively distant solid or liquid salt condensate, they are dependent on those condensates and their equilibrium vapor pressures, which are generally obtained in the volume immediately surrounding the condensate. Equilibrium vapor pressures for the salts of interest have rarely been measured for the relevant temperature range from 900 K to 1400 K. (Experimental difficulties posed by the relatively high pressures and temperatures are contributing factors to this situation.) Equilibrium vapor pressures are needed for numerical predictions of lamp performance based on detailed physical principals. Values for these parameters are currently obtained from *ab initio* calculations and from extrapolations of measurements made at lower temperatures. Lighting industry scientists would like to have at least some measurements to either correct or validate such values.

Vapor pressures are desired not only for pure salts such as DyI_3, TmI_3, HoI_3, ScI_3, etc., but also for *mixtures* of these salts with higher vapor pressure salts such as InI, TlI, CsI, etc. The latter are capable of significantly enhancing the presence of the former metals (Dy, Tm, Ho, Sc, etc.) in the vapor through hetero-complexing between the salt molecules.[2,3] For example, in a mixture of the salt SnI_2 and the much less volatile NaI, the vapor-phase reaction

$$NaI + SnI_2 \rightarrow NaSnI_3 \quad (1)$$

can lead to a substantial increase in the total density of Na in the vapor in the form of the complex $NaSnI_3$.[4] In such a case, SnI_2 is said to be a complexing agent that produces a

a)Electronic mail: jjcurry@nist.gov

volatility enhancement of NaI.[5,6] Similarly, volatility enhancements for lanthanides are expected in mixtures of lanthanide-iodides with volatile salts such as InI, TlI, CsI, and GaI_3.

We present measurements of the vapors in equilibrium with the salts DyI_3 and TmI_3, and salt mixtures DyI_3/InI and TmI_3/TlI, in the temperature range from 900 K to 1400 K. These measurements are significant, not only for the data obtained, but also because they were obtained using x-ray induced fluorescence (XRIF), a technique that has not previously been applied to this purpose. Some preliminary results from this effort have already been published,[7,8] but here we give additional results and make comparisons with calculated thermochemical equilibria. We also provide an improved absolute calibration that resolves previously reported discrepancies.

II. METHOD

We chose XRIF to study metal-halide vapors at high temperatures for several reasons. Among these are (1) compatibility with a closed system, (2) compatibility with the high vapor pressures relevant to MH-HID lamps, and (3) ability to obtain absolute measurements. A detailed description of the general technique is given in Ref. 9.

Working with high-energy photons generally facilitates all three of the preceding criteria. Photons with energy >20 keV will penetrate a few mm of polycrystalline alumina (PCA) or fused silica with acceptable attenuation. These materials were used to construct our vapor cells because of their long history of use in commercial lamps where similar conditions are obtained. Cross sections for photon-matter interactions are much smaller for photons with energies >20 keV than for optical photons, making it possible to measure vapors too dense for optical techniques. Finally, correlating x-ray intensities with particle densities is generally easier than with optical intensities.

In our measurements, we used monochromatic high-energy photons (61 keV or 86 keV) to produce K-shell (principal quantum number $n = 1$) ionization of the atoms constituting the molecules in the vapor. Such core ionization produces a highly excited ion with an empty core orbital. This excitation decays by an Auger process or emission of a photon. The fluorescence yield, or probability of stabilization by photon emission, is relatively large for K-shell ionization, being >50% for atoms heavier than Zn. Stabilization and fluorescence emission is the result of an electron from an outer shell $n > 1$ losing energy and filling the empty core orbital. The transition between bound orbitals gives the fluorescence a well-defined energy and the relatively simple spectral pattern created by different initial orbitals is sufficient to identify the atomic number of the emitter.

The intensity of K-shell fluorescence is dominated by $K_{\alpha 1}$ and $K_{\alpha 2}$ emission, which arise from initial orbitals in the L-shell ($n = 2$). These photons are only slightly lower in energy than the binding energy of the K-shell electrons. Decay of electrons from higher shells ($n > 2$) gives rise to less intense K_β, K_γ, K_η, etc., lines whose energies asymptotically approach the ionization energy.

In the case of a uniform, x-ray transparent vapor of atoms excited by a beam of monochromatic x rays, we postulate that the number of photons emitted per unit time per unit volume in K-shell fluorescence is

$$I^K = \frac{\Phi_i}{A_b}\,\sigma^K(E_i)\,Y^K\;\; n, \tag{2}$$

where Φ_i is the incident photon flux, A_b is the beam cross-sectional area, $\sigma^K(E_i)$ is the K-shell photo-absorption cross section at the energy of the incident photons E_i, Y^K is the K-shell fluorescence yield, and n is the volume density of atoms. Equation (2) demonstrates the linear relationship between fluorescence intensity and both the total density of atoms and the incident beam intensity. The atomic parameters σ and Y are generally known to better than 10%, except in the easily avoided situation where the incident photon energy is close to the K-shell ionization energy. The energy dependence of σ on E_i is relatively weak compared to that for optical resonances and thus, there are typically no difficulties with stabilizing and determining the incident photon energy.

X-ray fluorescence energies are a function of atomic number Z. The intensity of a particular K-shell fluorescence line can be written as[10]

$$I_Z^{K\eta} = \frac{\Phi_i}{A_b}\,\sigma_Z^K(E_i)\,Y_Z^K\;\; B_Z^{K\eta}\;\; n_Z, \tag{3}$$

where $K\eta$ ($\eta = \alpha 1, \alpha 2, \beta 1, \ldots$) signifies a particular K-shell line and $B^{K\eta}$ is the probability of emission of a $K\eta$ photon relative to the sum of all K-shell lines. The Z in the subscript to the density n signifies that the emitted intensity is proportional to the *total* density of atoms of atomic number Z regardless of chemical state, i.e.,

$$n_Z = \sum_i c_{Zi} M_i \tag{4}$$

is the sum over all i atomic and molecular species M, where the stoichiometric coefficient c_{Zi} is the number of atoms of atomic number Z in molecule M_i.

There is a small energy dependence of the emitted fluorescence on chemical state, the so-called chemical shift. This energy (chemical bond energy) is typically on the order of a few eV or less and is not resolved in our measurements.

We define a vapor pressure corresponding to the measured total density of element Z as

$$p_Z = n_Z kT = kT \sum_i c_{Zi} M_i, \tag{5}$$

where k is Boltzmann's constant and T is the measured temperature of the vapor. This pressure should not be confused with an actual total or partial pressure since c_{Zi} is, in general, greater than 1. Thus, the validity of the Ideal Gas Law as a virial equation under our experimental conditions is an unrelated question. The primary virtue of this definition is that it corresponds directly to the measured value n_Z and, just as importantly for lighting applications, it is a measure of the total quantity of a given element in the vapor.

The dominant uncertainties in the model embodied by Eqs. (2) and (3) are the accuracies with which the atomic parameters are known. These are discussed further in Sec. VI.

The effect of inaccuracies in the parameters is minimized by relying on ratios of these parameters, as discussed in Sec. III.

III. EXPERIMENT

Our measurements were conducted at the Advanced Photon Source, Argonne National Laboratory on the Sector 1 Insertion Device Beam Line. Figure 1 gives a schematic layout of the experiment. A highly collimated, monochromatic x-ray beam, produced by the Sector 1 double crystal monochromator,[11] is shown entering from the right, transiting the vapor cell, and exiting the experiment to the left. X-ray fluorescence induced in the vapor was observed perpendicular to the incident beam by a solid-state germanium detector, shown at the bottom of the figure. A set of adjustable crossed slits trimmed the beam size to 500 μm × 500 μm. Following the slits, a nitrogen-filled ionization chamber continuously monitored the flux incident on the vapor cell. A second ionization chamber after the cell monitored the transmitted flux.

The energy spread of the beam photons is sufficiently small that the photo-electric cross section $\sigma_Z^K(E_i)$ appearing in Eq. (3) is single-valued and no integration over energy is required. The angular divergence of the beam, though different in the horizontal and vertical planes, is $<20\,\mu$rad in both cases. The flux in the trimmed beam was on the order of 10^{12} s^{-1}, but measurement of its absolute value is not required.

Each of the salts/salt mixtures to be examined was contained in a permanently sealed vapor cell made of polycrystalline alumina. The cell geometry, Figure 2, was designed to minimize Compton scattering, as discussed in Ref. 9. It is cylindrically symmetric about the axis shown, except for the filling capillary at the top of the figure. This capillary was used for evacuating the cell and introducing the desired salt(s) and/or rare gas. A PCA rod was then frit-sealed into the stem as close to the body of the cell as possible.

The vapor cell was placed in a tantalum jacket as shown in Figure 3 in order to minimize the number of scattered photons reaching the detector and to provide a more uniform temperature distribution on the surface of the cell. The jacket was also cylindrically symmetric, except for a hole to accommodate the capillary, a hole to allow the escape of fluorescence photons, and a pair of holes into which thermocouples were inserted.

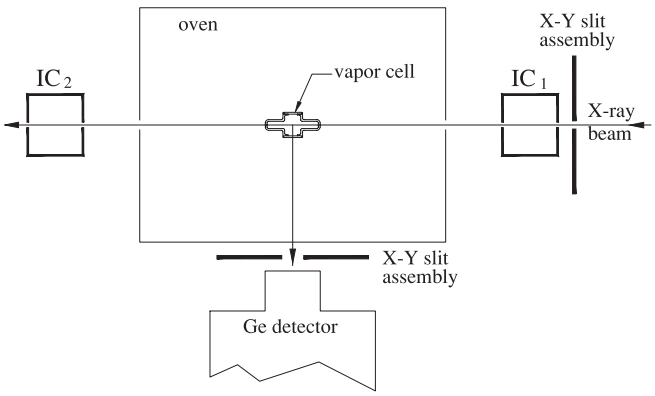

FIG. 1. Schematic of experiment for measuring vapor-phase densities with x-ray induced fluorescence. IC_1 and IC_2 are upstream and downstream ionization chambers for non-perturbatively measuring the photon flux in the x-ray beam.

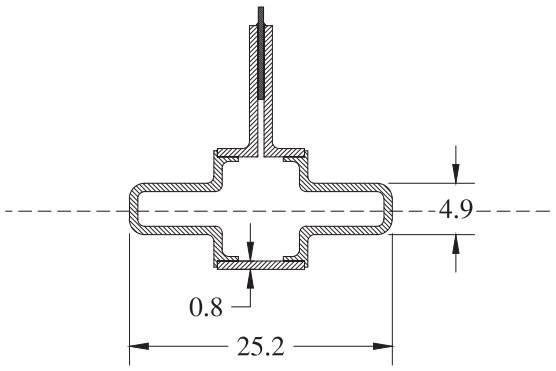

FIG. 2. Cross section of a PCA vapor cell, with dimensions in millimeters. The cell is cylindrically symmetric about the axis shown except for the capillary at the top.

The tantalum jacket/vapor cell assembly was inserted into the oven[9] as shown in Figure 4. The heating element in the oven was driven by a direct current power supply, with a nitrogen purge preventing oxidation of metal components.

The limiting apertures for collection of photons by the detector were the hole in the tantalum jacket (1.23 mm or 1.59 mm, depending on the jacket used) and the X-Y slit assembly in front of the detector (6 mm × 2 mm). The latter was adjusted to optimize the ratio of fluorescence photons to scattered photons reaching the detector. Although fluorescence is induced in the vapor along the length of the beam, the limiting apertures restricted the detector's field-of-view to a length only slightly longer than the diameter of the hole in the jacket.

The number of counts C recorded by the detector in one of the K-shell fluorescence lines η of element Z is

$$C_Z^{K\eta} = I_Z^{K\eta}\,\frac{\Omega}{4\pi}\,V\,\tau(E_i)\,\tau\left(E_Z^{K\eta}\right)\,Q_d\left(E_Z^{K\eta}\right), \qquad (6)$$

where Ω is the solid angle observed by the detector, V is the volume of the incident beam falling within the field-of-view of the detector, τ is the transmission of x rays of fluorescence energy $E_{K\eta}$ through the vapor cell wall, and Q_d is the detector efficiency.

The difficulty with using Eq. (6) to determine absolute densities lies with the geometric factor ΩV, which more

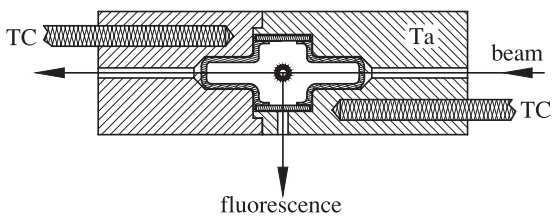

FIG. 3. Vapor cell jacketed by tantalum. The latter absorbed scattered x rays and provided a more uniform temperature distribution over the cell. Here the cell has been rotated, relative to Figure 2, about the beam axis so that the capillary points out of the page. Thermocouples were inserted into two holes in the tantalum, one in the upper left and one in the lower right. A small hole, shown at the bottom of the figure, allowed x-ray fluorescence to escape toward the Ge detector.

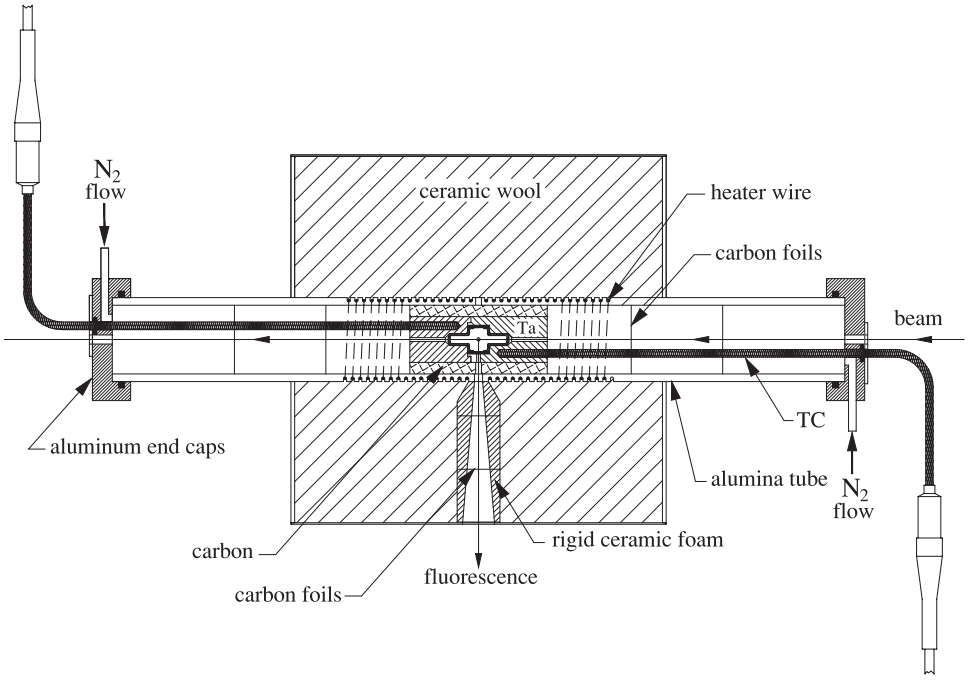

FIG. 4. The vapor cell and tantalum jacket positioned in the tube furnace. The heating element is a spiral-wound resistive wire driven by direct current. Carbon foils reduce heat loss by convection along the tube and through the fluorescence exit hole. A nitrogen purge prevents oxidation.

correctly should be $\int_V \Omega \, dV$. While all the other terms in Eq. (6) can be calculated with sufficient accuracy, the geometric term is much more difficult and necessitates a calibration. The calibration is achieved by substitution of a standard in place of the vapor cell to be measured. The standard is an identical vapor cell filled only with 380(±40) Pa of Xe. Using Eqs. (3) and (6), the unknown density is determined from the product of a number of ratios

$$n_Z = \frac{C_Z^{K\eta}}{C_{Xe}^{K\alpha}} \frac{\Phi_i(Xe)}{\Phi_i(Z)} \frac{\sigma_{Xe}^K(E_i)}{\sigma_Z^K(E_i)} \times \frac{Y_{Xe}^K}{Y_Z^K} \frac{B_{Xe}^{K\alpha}}{B_Z^{K\eta}} \frac{\tau\left(E_{Xe}^{K\alpha}\right)}{\tau\left(E_Z^{K\eta}\right)} \frac{Q_d\left(E_{Xe}^{K\alpha}\right)}{Q_d\left(E_Z^{K\eta}\right)} n_{Xe}. \quad (7)$$

In this manner, a number of potential systematic errors are eliminated. The relative number of counts, the relative beam flux, and the Xe density are measured, while the remaining ratios can be determined from tabulated values.[12–14]

Table I gives a summary of the vapor cells and salt chemistries examined, while Table II gives details of the Xe-filled cells.

Two typical XRIF spectra in Figure 5 contain fluorescence peaks for all of the elemental components of the corresponding salt(s). K-shell lines are labeled for each element. Some of the lines are blended, as is the case for the Kα1 and Kα2 lines of In and I. These two lines are partially resolved for Dy and Tm, while for Tl they are fully resolved. Number densities are obtained by integrating the counts contained in one or more peaks corresponding to each element.

TABLE I. Details of observed vapor cells. The cell volume is 7.3(±0.7) × 10^{-7} m^{-3}.

Cell no.	Salt mixture	Target quantities (mg)	Simulated quantities (mg)	Simulated mole fraction[a]	Beam energy (keV)
1	DyI_3[b,c]	10.3	10.3/0.0013[d]	2.8×10^{-4}	86
3	DyI_3/InI[b,e]	11.8/0.72	11.8/0.9	0.14	86
4	DyI_3/InI[b,e]	12.5/0.71	11.8/0.9	0.14	61
5	TmI_3[b,c]	8.9	8.9	...	86
8	TmI_3/TlI[b,e]	8.8/0.63	6.0/0.76	0.17	86

[a]Of minority component.
[b]Also nominally contains 670 Pa of Ar at 295 K.
[c]Some data previously reported in Ref. 7.
[d]DyI_3/InI.
[e]Some data previously reported in Ref. 8.

IV. THERMOCHEMICAL EQUILIBRIUM MODEL

We have also used numerical modeling of the thermochemical equilibrium within each test cell to interpret our measurements, including the importance of various molecular species and the compatibility of existing thermochemical data with our results.

Our model, based on the algorithm of Cruise,[15] utilizes the free energies of formation of all molecular species to

TABLE II. Details of Xe-filled cells.

Cell no.	Target quantity (Pa)[a]	Measured quantity (Pa)[a]	Beam energy (keV)
A3	670	380(±40)	61, 86
B2[b]	100	...	61

[a]At standard temperature, 273 K.
[b]Not used for calibration.

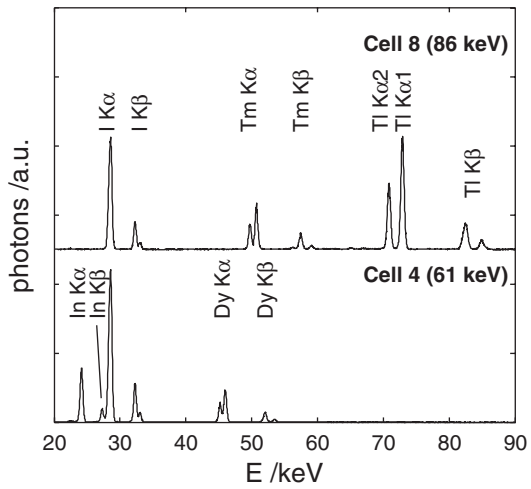

FIG. 5. Two typical fluorescence spectra from a cell containing DyI_3/InI and a cell containing TmI_3/TlI. Number densities are obtained by integrating the counts contained in one or more peaks corresponding to each element.

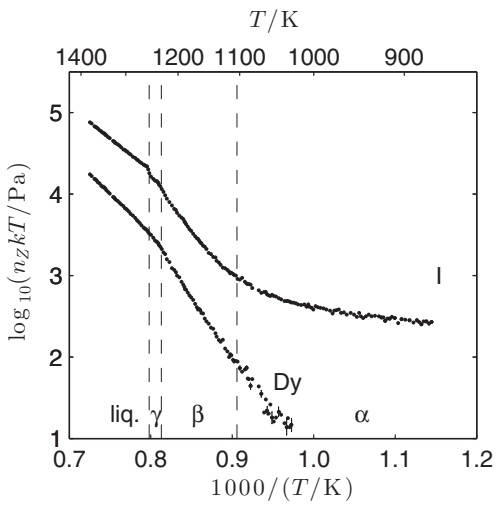

FIG. 6. Measured vapor pressures corresponding to total vapor densities of Dy and I for cell 1 nominally containing only 10.3 mg of DyI_3.

compute a self-consistent set of the numbers of each molecule in a closed system. Assumptions are pure solids, ideal liquid solutions, and ideal vapors. For the highest temperatures investigated, the total pressures in our calculations approach, but do not exceed, 10^5 Pa where non-ideal behavior begins to become apparent. Input parameters are temperature, cell volume, salt dose in the cell, and free energies of formation ($\Delta_f G^\circ(T)$) of all molecular phases to be considered.

We utilized published values for the free energies of formation whenever possible. For consistency, we used the JANAF tables[16] as our primary source. When sought after values could not be found in the JANAF tables, we turned to Barin's compilations,[17] and if necessary to other sources. Where no published values exist, we used the model and data to infer values for the free energies of formation, as described in Sec. V.

V. RESULTS AND DISCUSSION

Vapor pressures corresponding to the total densities of Dy and I in cell 1 (dosed with 10.3 mg of DyI_3) are shown in Figure 6. (These and all other measured pressure values are available in the supplementary material.[18]) DyI_3 has been shown to have three solid phases (α, β, and γ).[19] The temperature ranges where these and the liquid phase are stable are indicated by vertical dashed lines in Figure 6. Statistical uncertainties arising from fluctuations in the spectral data only are shown for a few Dy points. At the lowest values for both species, those uncertainties are ±40%, but decrease rapidly with increasing vapor pressure and are less than ±1% at the highest vapor pressures. The measured vapor pressure values given in Figure 6 are approximately 40% less than those reported earlier.[7,8] The difference is due to our recent measurement of the Xe pressure in the calibration cell A3, showing the actual pressure to be 380(±40) Pa instead of the target pressure of 670 Pa.

To simulate a system identical to the one we observed, we included the species DyI_3(s,l,v) (s≡solid, l≡liquid, and v≡vapor), as well as the vapor-phase dimer Dy_2I_6, which has been observed by multiple investigators.[20–22] The free energy of formation $\Delta_f G^\circ$ for DyI_3(v) was obtained from Barin,[17] while the logarithm of the equilibrium constant $\log_{10}(K_d)$ for the reaction,

$$2\mathrm{DyI_3(v)} \leftrightarrow \mathrm{Dy_2I_6(v)}, \tag{8}$$

was obtained from Ohnesorge.[22] The combination of the two allowed us to determine the free energy of formation of the dimer using the relation

$$\log_{10}(K_\mathrm{d}) = \frac{2\Delta_f G^\circ[\mathrm{DyI_3(v)}] - \Delta_f G^\circ[\mathrm{Dy_2I_6(v)}]}{\ln(10)RT}. \tag{9}$$

We obtained the partial pressure of the dimer p_d by expressing both the equilibrium constant K_d and our measured values p_{Dy} in terms of the partial pressures of monomer p_m and dimer

$$K_\mathrm{d} = \frac{p_\mathrm{d}}{p_\mathrm{m}^2}, \tag{10}$$

$$p_\mathrm{Dy} = p_\mathrm{m} + 2p_\mathrm{d}. \tag{11}$$

Here, pressures are expressed in units of standard pressure or 10^5 Pa. The measured vapor pressure p_{Dy} corresponding to the total density of Dy, along with the derived monomer and dimer partial pressures are given in Figure 7. Also shown, by the solid line, is the expression given by Hansen *et al.*[23] for the vapor pressure of DyI_3 in equilibrium with the solid condensate. The expression given by Hansen *et al.*[23] was obtained at lower temperatures where the dimer fraction should be insignificant. In the temperature range from 1100 K to 1200 K, it is a good approximation to the vapor pressure corresponding to the *total* density of Dy.

Free energies of formation for the β, γ, and liquid phases of DyI_3 were obtained from that of DyI_3(v) and least-squares fits to the measured data using relationships analogous to Eq. (9). The free energy of formation for the α phase could not be established in this manner because our measurements

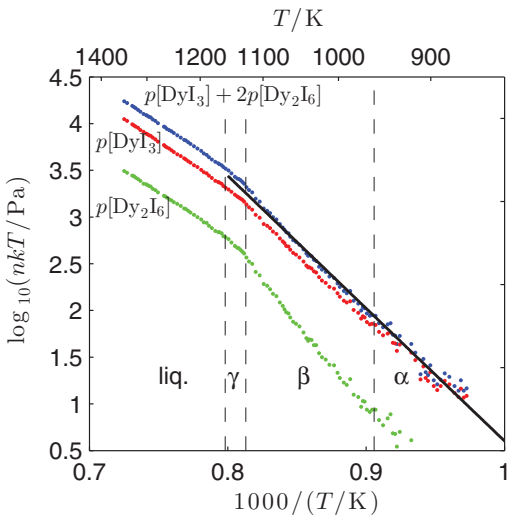

FIG. 7. Measured vapor pressure (blue) corresponding to the total vapor density of Dy in cell 1 nominally containing only 10.3 mg of DyI_3. These values are the sum of the vapor pressure of the DyI_3 monomer (red) and twice the Dy_2I_6 dimer (green). The expression given by Hansen *et al.*[23] for the vapor pressure of DyI_3 is shown by the solid line.

for Dy did not extend far enough into the temperature range where the α phase is stable. In our calculations, we used the free energy of formation for the β phase to describe the α phase. Analytic expressions for all of the free energies of formation used in the model are given in Table III.

The numerical model, using the species and free energies discussed above, closely matches the measurements for Dy as expected and as shown in Figure 8 by the red curves. The agreement is excellent because we used the data to derive free energies of formation from the measured vapor pressure values.

Despite the excellent agreement for Dy, the model does not reproduce the observed vapor pressure corresponding to the total density of I. The measurements indicate an I:Dy ratio greater than the 3:1 ratio of the species used in the model. Part of the discrepancy can be explained by a small amount of contamination in the vapor cell. In fact, weak fluorescence from In is observed in the x-ray spectra. In addition, optical fluorescence from hydrogen is observed when the cell is excited, at room temperature, by a high-frequency electric field. (Lanthanide salts are extremely hygroscopic and minute water contamination is common in metal-halide lamps. Minor quantities of water may also originate from outgassing of the frit used to seal the vapor cells.) Figure 9 shows revised calculations when 900 ng of InI and 150 ng of water are added to the 10.3 mg of DyI_3. The molecular species InI(s,l,v), InI_2(v), InI_3(s,l,v), I(v), I_2(s,l,v), $DyInI_4$(v), H_2O(l,v), H_2O_2(v), H(v), H_2(v), HI(v), O_2(v), O(v), In_2O(v), In_2O_3(s), and Dy_2O_3(s) are allowed in addition to the species included in the first calculation. The free energies of formation for all of these additional species are obtained from compilations of thermodynamic data,[16,17] except that for the complex $DyInI_4$(v), which was obtained by combining Ohnesorge's value[22] for the equilibrium constant corresponding to the reaction

$$DyI_3(v) + InI(v) \leftrightarrow DyInI_4(v), \quad (12)$$

with the free energies of formation for DyI_3(v) and InI(v) in the same manner as we obtained the free energy of formation for Dy_2I_6(v). All of these free energies of formation are given in Table III.

Water in the cell leads to the reaction

$$2DyI_3(s) + 3H_2O(l) \leftrightarrow Dy_2O_3(s) + 6HI(v), \quad (13)$$

with HI providing extra iodine in the vapor. The amount of Dy in the vapor is not affected significantly by this reaction, or by the small amount of InI present as a contaminate. InI reacts with free I to form InI_3 at low temperatures, another source of I in the vapor.

The reactions discussed above do not entirely explain the magnitude of the I measurements. It is tempting to attribute the discrepancy to a systematic experimental error since a factor of 1.6 would bring the two into a better global agreement. However, data for all elements are acquired simultaneously with the same detector, so the relative scaling is robust. Furthermore, the details of the I curve would not be matched by a simple scaling. In particular, the I density above the melting point of DyI_3 is growing at a smaller rate than the corresponding curve for the calculations, which reflect the 3:1 stoichiometric ratio of DyI_3. The measurements give an I:Dy ratio that varies from 5.7 down to 4.2 and suggests the presence of another I-containing species with a different stoichiometric ratio to Dy. Visual examination of the vapor cells after the measurements do not show evidence of reactions involving the cell wall.

Figure 10 shows measurements from cells 3 and 4, the two cells nominally containing the same mixture of DyI_3 and InI. The discrepancy between these two cells reported earlier[8] has been resolved by our discovery that cell 3 measurements were made with an alternative tantalum jacket whose fluorescence hole diameter measured 1.59 mm instead of the 1.23 mm of the jacket used for all the other cells. The close agreement now seen in the measurements from these two cells indicates, not only a close match in the doses of the two cells, but also the reproducibility of the measurement method.

The vapor pressure corresponding to the total density of Dy measured in cell 1 is also shown in Figure 10 for comparison. The strong enhancement of the vapor pressure corresponding to the total density of Dy seen in the cells containing InI indicate the formation of one or more Dy-In complexes. As discussed earlier, Ohnesorge[22] observed $DyInI_4$(v) in the mixed salt system and determined the equilibrium constant for its formation from DyI_3(v) and InI(v). We simulated a mixed salt system containing 11.8 mg of DyI_3 and 0.71 mg of InI allowing the species DyI_3(α,β, γ,l,v), InI(s,l,v), InI_3(s,l,v), InI_2(v), I_2(s,l,v), I(v), Dy_2I_6(v), and $DyInI_4$(v). The results are shown by the red curves in Figure 10, and there are major differences with the observations.

The primary difference between our calculations and measurements is the much larger pressures corresponding to In and I given by the model. In the model, the quantity of In and I in the vapor at lower temperatures is dictated by the equilibrium vapor pressure of pure InI because DyI_3 remains solid and there is no mechanism in the model for interactions between the two salts. The relatively small dose of InI evaporates completely at a temperature just above 900 K, leaving

TABLE III. Free energies of formation used in thermochemical equilibrium calculations for systems containing DyI_3 over the temperature range from 800 K to 1400 K.

Molecule	$\Delta_f G^\circ(T)$ /(J/mol)[a]	Source
DyI_3(s, α, and β)	$-430\,400 - 291.8\,T + 0.2864\,T^2 - 3.841 \times 10^{-5}\,T^3$	Present measurements[b]
DyI_3(s,γ)	$-652\,900 + 194.0\,T - 1.557 \times 10^{-2}\,T^2 + 5.874 \times 10^{-6}\,T^3$	Present measurements[b]
DyI_3(l)	$-619\,400 + 167.4\,T - 1.557 \times 10^{-2}\,T^2 + 5.874 \times 10^{-6}\,T^3$	Present measurements[b]
$DyIn_2I_5$(l)	$-823\,600+128\,T$	Present measurements[b]
DyI_3(v)	$-430\,400 + 48.60\,T - 1.557 \times 10^{-2}\,T^2 + 5.874 \times 10^{-6}\,T^3$	Barin[17]
Dy_2I_6(v)	$-1\,056\,000 + 231.3\,T - 3.114 \times 10^{-2}\,T^2 + 1.175 \times 10^{-5}\,T^3$	Ohnesorge[22] and Barin[17]
$DyInI_4$(v)[c]	$-626\,300+115.9\,T - 1.557 \times 10^{-2}\,T^2 + 5.874 \times 10^{-6}\,T^3$	Ohnesorge[22] and Barin[17]
$DyInI_4$(v)[d]	$-370\,300-360\,T + 0.2\,T^2$	Present measurements[b]
Dy_2O_3(s)	$-1\,849\,000 + 276.9\,T$	Barin[17]
InI(s)	$-148\,700 + 67.94\,T$	Barin[17]
InI(l)	$-126\,100 + 32.15\,T$	Barin[17]
InI(v)	$-35\,300-57.90\,T$	Barin[17]
InI_2(v)	$-91\,000-23.33\,T + 3.844 \times 10^{-3}\,T^2$	Barin[17]
InI_3(s)	$2000-1121\,T+1.406\,T^2$	Barin[17]
InI_3(l)	$-290\,100 + 159.6\,T$	Barin[17]
InI_3(v)	$-219\,700 + 60.24\,T$	Barin[17]
In_2O(v)	$-77\,750-56.60\,T + 7.076\times 10^{-3}\,T^2$	Barin[17]
In_2O_3(s)	$-921\,800 + 317.4\,T$	Barin[17]
I(v)	$78\,190-53.82\,T$	JANAF tables[16]
I_2(s)	$-5383-39.48\,T + 0.1352\,T^2$	JANAF tables[16]
I_2(l)	$-46\,920 + 116.4\,T - 0.03018\,T^2$	JANAF tables[16]
I_2(v)[e]	0	JANAF tables[16]
H_2O(l)	$-283\,300 + 155.2\,T$	JANAF tables[16]
H_2O(v)	$-241\,200 + 43.41\,T + 4.959 \times 10 - 3\,T^2$	JANAF tables[16]
H_2O_2(v)	$-140\,300 + 111.8\,T$	JANAF tables[16]
H(v)	$222\,100-56.87\,T$	JANAF tables[16]
H_2(v)[f]	0	JANAF tables[16]
HI(v)	$-6517-7.211\,T$	JANAF tables[16]
O_2(v)[g]	0	JANAF tables[16]
O(v)	$252\,300-64.80\,T$	JANAF tables[16]

[a]The reference states for all species are the elements in their most stable state at the given temperature.
[b]Obtained by optimizing agreement between calculations and present measurements.
[c]Used in calculations for cell 1.
[d]Used in calculations for cells 3 and 4.
[e]I_2(v) is the reference state for $T > 458$ K.
[f]H_2(v) is the reference state for $T > 20$ K.
[g]O_2(v) is the reference state for $T > 90$ K.

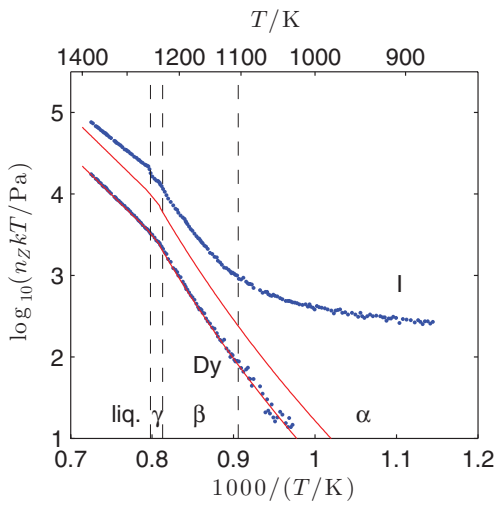

FIG. 8. Measured vapor pressures (blue) corresponding to the total densities of Dy and I in cell 1 nominally containing 10.3 mg of DyI_3 compared with calculations (red).

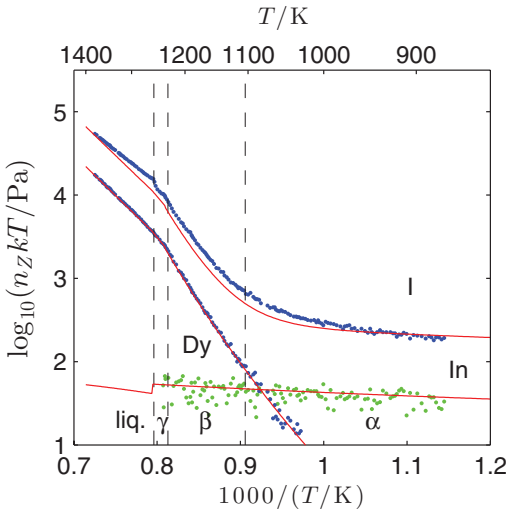

FIG. 9. Measured vapor pressures corresponding to the total densities of Dy (blue), I (blue), and In (green) in cell 1 nominally containing only 10.3 mg of DyI_3 compared with calculations (red) for 10.3 mg of DyI_3, 900 ng of InI, and 150 ng of H_2O.

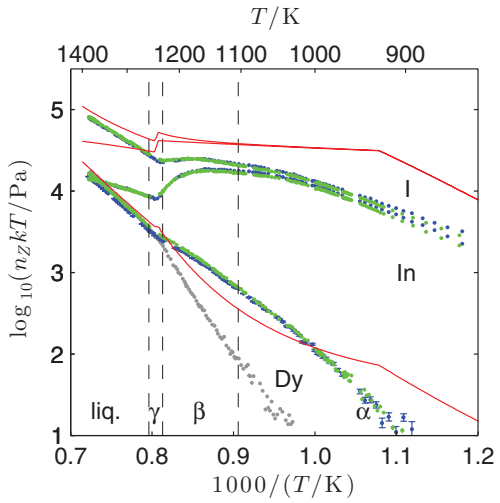

FIG. 10. Measured vapor pressures corresponding to the total densities of Dy, In, and I in cell 3 (green) nominally containing 11.8 mg of DyI_3 with 0.72 mg of InI and cell 4 (blue) nominally containing 12.3 mg of DyI_3 with 0.71 mg of InI. Measurements of the vapor pressure corresponding to the total density of Dy from cell 1 are shown in gray. Calculations for 11.8 mg of DyI_3 with 0.71 mg of InI are shown in red.

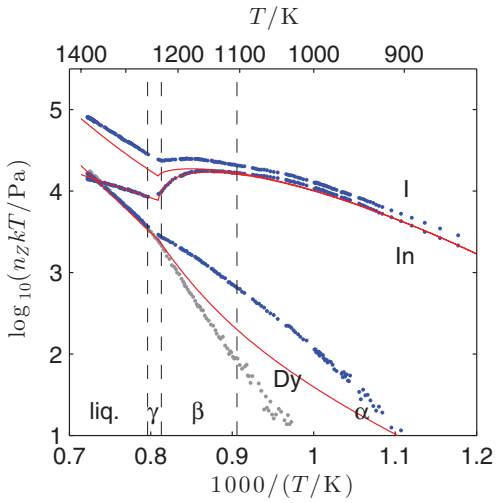

FIG. 11. Measured vapor pressures (blue) corresponding to the total densities of Dy, In, and I in cell 4. Calculations (red) are for 11.8 mg of DyI_3 with 0.9 mg of InI and include the liquid phase complex $DyIn_2I_5$. Measurements of the vapor pressure corresponding to total density of Dy in cell 1 are shown in light gray.

behind a pure DyI_3 solid condensate. Complete evaporation is the origin of the discontinuity in the slope of the vapor pressure curves.

The measured vapor pressure corresponding to the total density of In, on the other hand, is well below the equilibrium vapor pressure for pure InI. Without melting of DyI_3, and assuming no impurities, this requires an interaction between the two salts in the condensed phase. Formation of a hetero-complex, $DyInI_4$(l), for example, would reduce the total quantity of In in the vapor by suppressing the evaporation of InI (by dilution[24]) if the complex has a lower vapor pressure than InI. The suppression of evaporation has the additional effect that an InI melt persists to higher temperatures. The measurements indicate that an InI melt remains to temperatures high enough that DyI_3 begins to melt, further diluting InI(l). Apparently, as more DyI_3 melts, InI rapidly becomes a minor component of the melt, even while it remains a major component of the vapor. The effect of dilution with increasing temperature overwhelms the usual increase in vapor pressure. This is the origin of the strong decrease in In content (and to a smaller extent in I) with increasing temperature, which practically terminates when all of the DyI_3 melts at the normal melting temperature of the pure salt (around 1260 K).

In fact, simulations including the liquid-phase complex $DyIn_2I_5$(l), instead of $DyInI_4$(l), are better able to reproduce our observations of the DyI_3/InI system. The free energy of formation for $DyIn_2I_5$(l) that gives the closest match to the measurements is given in Table III. We also improved the match by using a larger dose of InI: 0.9 mg instead of 0.71 mg. The results are shown in Figure 11.

The addition of the liquid phase complex explains the behavior of In quite well, but its addition increases disagreement with the measured vapor pressure corresponding to Dy by further lowering the simulated value of that pressure. One or more additional vapor phase complexes could resolve this discrepancy. $DyInI_4$(v) is capable of resolving the disagreement if its free energy of formation is *optimized* to fit our measurements rather than *derived* from the free energies of formation of DyI_3(v) and InI(v),[17] and the equilibrium constant for the complex formation given by Ohnesorge,[22] as we did earlier. Figure 12 shows both the optimized and derived free energies of formation, with the latter being shown only for the temperature range for which Ohnesorge[22] had data. The two functions cross in this region, although the slopes and curvatures are distinctly different. Both the optimized and derived values are given in Table III.

Figure 13 compares simulations with measurements when the optimized free energy of formation is used for $DyInI_4$(v). There is now good agreement everywhere, and excellent agreement in many places. To summarize, the steps taken to achieve this agreement were (1) postulation of $DyIn_2I_5$ liquid complex, (2) increase in the dose of InI to 0.9 mg, and (3) adjustment of the free energy of formation of $DyInI_4$(v). Both measurements and simulations agree that

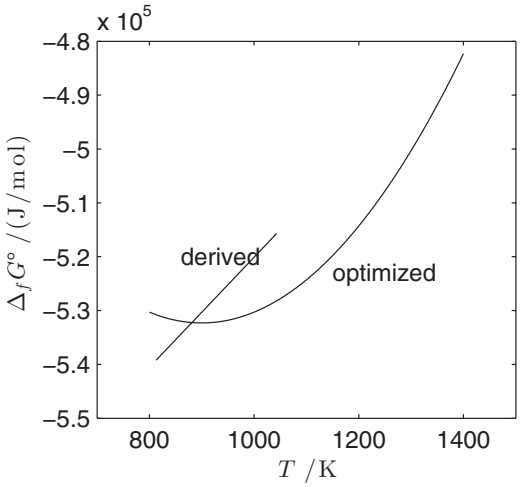

FIG. 12. Derived and optimized free energies of formation for $DyInI_4$(v).

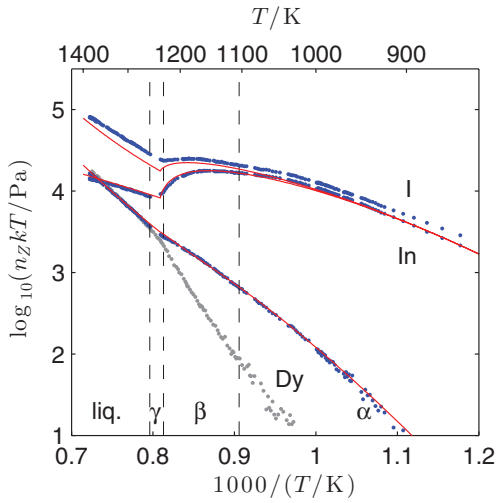

FIG. 13. Measured vapor pressures (blue) corresponding to the total densities of Dy, In, and I in cell 4 nominally containing 12.5 mg of DyI_3 and 0.71 mg of InI. Predictions from the thermochemical equilibrium model (red) include the liquid phase complex $DyIn_2I_5$ and an optimized $\Delta_f G^\circ$ for $DyInI_4$(v) with 11.8 mg of DyI_3 and 0.9 mg of InI. Measurements of the vapor pressure corresponding to total density of Dy in cell 1 are shown in light gray.

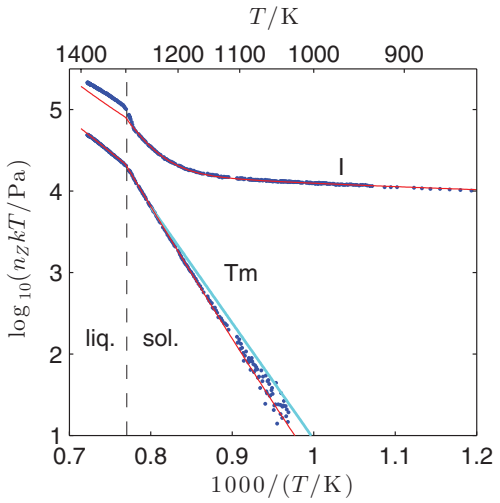

FIG. 14. Measured vapor pressures (blue) corresponding to the total vapor densities of Tm and I in cell 5 nominally containing 8.9 mg of TmI_3 compared with calculations (red) for a cell containing 8.9 mg of TmI_3 and 4.9 μg of H_2O. The expression given by Hansen *et al.*[23] for the equilibrium vapor pressure of TmI_3(v) is shown by the cyan line.

the enhancement of the Dy content in the vapor disappears at or near the melting point of DyI_3(s), regardless of which free energy of formation is used for $DyInI_4$(v).

The free energies of formation used in the thermochemical calculations and given in Table III cannot be considered measured values. The specified species and free energy values are mathematically possible and mathematically simple solutions to the problem of matching calculations to observed measurements. They are undoubtedly not unique, and may not even be physically realistic solutions, at least as far as the temperature dependence of the free energies are concerned. There are still lingering discrepancies, although modest, especially with I, as already noted. Furthermore, most of the free energy of formation values proposed here are dependent on other published free energy values or equilibrium constants whose uncertainties have generally not been adequately tested. The values in Table III are instead given so that the modeling results can be reproduced if desired. The conclusions that can and should be drawn from this exercise are (1) one or more liquid complexes are likely a major factor in determining the vapor phase content, and (2) the enhancement of Dy in the vapor is stronger than that predicted by Ohnesorge's value for the equilibrium constant of the formation of $DyInI_4$(v).

Our analysis of the TmI_3 and TmI_3/TlI systems proceeded in the same manner as just described for the DyI_3 and DyI_3/InI systems. Measurements of the TmI_3 system are shown in Figure 14, along with the expression given by Hansen *et al.*[23] for the equilibrium vapor pressure of TmI_3(v) based on measurements made at 1110 K and below. Also shown, are calculations for 8.9 mg of TmI_3 and 4.9 μg of H_2O, allowing the species TmI_3(s,l,v), Tm_2I_6(v), I_2(s,l,v), I(v), H_2O(l,v), H_2(v), H(v), HI(v), O_2(v), O(v), H_2O_2(v), and Tm_2O_3(s). Free energies of formation for species not given in Table III are given in Table IV, along with their sources. We included H_2O in these calculations to account for the high pressure of I at temperatures below 1100 K. Our measurements for the vapor pressure corresponding to the total density of Tm are slightly less than the expression given by Hansen *et al.* for the TmI_3 vapor pressure in the temperature range from 1100 K to 1200 K.

The free energy of formation for the Tm dimer derived from Dettingmeijer and Dielis[25] results in the partial pressure of Tm_2I_6(v) being larger than the partial pressure of the monomer TmI_3(v) for $T > 1050$ K up to the maximum temperature investigated. This contrasts with DyI_3 where the dimer partial pressure was shown to be always much less than that of the monomer (see Figure 7). As a consequence, the free energies of formation for both TmI_3(s) and TmI_3(l), which we derived from our measurements and the partial pressure of the monomer, are greatly affected. (This is true to a lesser extent for the other free energies of formation derived from our measurements.) Karwath, Kobertz, and Hilpert,[26] also made measurements of the monomer and dimer partial pressures over a TmI_3 condensate, but with roughly a factor of two lower dimer fraction. If we had derived $\Delta_f G^\circ$(dimer) on the latter data, our values for the free energies of formation for TmI_3(s) and TmI_3(l) would have been $-680\,700 + 203.0\,T + 4.189 \times 10^{-3}\,T^2$ J/mol and $-586\,500 + 130.5\,T + 4.189 \times 10^{-3}\,T^2$ J/mol, respectively.

Measurements and simulations of the TmI_3/TlI system are shown in Figure 15. The simulations used 6.0 mg of TmI_3, 760 μg of TlI, and 4.2 μg of H_2O. In addition to those species allowed in the simulation of the pure TmI_3 system, this simulation included TlI(s,l,v), Tl_2I_2(v), $TmTlI_4$(l,v), and $TmTl_2I_5$(l). Barin's free energies of formation for TlI are not compatible with the vapor pressure for TlI over the solid and liquid phases. Therefore, we derived free energies of formation for the solid and liquid phases from Barin's values for the vapor and expressions given by Hansen *et al.*[23] for the vapor pressures over the solid and liquid.

Two complexes in the liquid phase and one complex in the vapor phase were required to match the data as well as

TABLE IV. Free energies of formation used in thermochemical equilibrium calculations for systems containing TmI_3 and not appearing in Table III. The calculations extended over the temperature range from 800 K to 1400 K.

Molecule	$\Delta_f G^\circ(T)$ /(J/mol)[a]	Source
TmI_3(s)	$-670\,200 + 190.2\,T + 4.189\times 10^{-3}\,T^2$	Present measurements[b]
Tm_2O_3(s)	$-1\,879\,000 + 292.4\,T$	Barin[17]
TmI_3(l)	$-581\,200 + 121.8\,T + 4.189\times 10^{-3}\,T^2$	Present measurements[b]
$TmTlI_4$(l)	$-683\,000 + 110\,T$	Present measurements[b]
$TmTl_2I_5$(l)	$-804\,000 + 210\,T$	Present measurements[b]
TmI_3(v)	$-420\,900 + 29.08\,T + 4.189\times 10^{-3}\,T^2$	Barin[17]
Tm_2I_6(v)	$-1\,011\,000+146.8\,T + 8.378\times 10^{-3}\,T^2$	Dettingmeijer and Dielis[25]
$TmTlI_4$(v)	$-607\,000 + 60\,T$	Present measurements[b]
TlI(s)	$-160\,700 + 54.89\,T + 5.988\times 10^{-3}\,T^2$	Barin[17] and Hansen et al.[23]
TlI(l)	$-139\,100 + 25.63\,T + 5.988\times 10^{-3}\,T^2$	Barin[17] and Hansen et al.[23]
TlI(v)	$-29\,090$-$74.74\,T + 5.988\times 10^{-3}\,T^2$	Barin[17]
Tl_2I_2(v)	$-150\,300$-$27.30\,T + 0.01198\,T^2$	Ohnesorge[22] and Barin[17]

[a]The reference states for all species are the elements in their most stable state at the given temperature.
[b]Obtained by optimizing agreement between calculations and present measurements.

shown in Figure 15 while still maintaining relatively simple free energy of formation functions. Water accounted for the extra I seen at low temperatures. In both the TmI_3 and TmI_3/TlI systems, there is a distinct increase in the vapor pressure corresponding to the total density of I at or near the melting temperature of TmI_3 that we are unable to reproduce with the species listed. As with the DyI_3/InI system, the enhancement of Tm in the vapor of Tm_3/TlI disappears at or near the melting point for TmI_3 and above.

In all of our measurements there have been discrepancies between the measured and calculated values for I. However, the discrepancies have had distinctly different features in each case, leading one to dismiss a systematic cause. Undetected spectral blends with the iodine K_α fluorescence line are unlikely, as the spectral resolution of our detector is sufficient to see the presence of lines from different elements. Where these discrepancies occur, the measured values are larger than the calculated values, suggesting some combination of (1) dissociation of the metal-iodides, (2) metal-iodides other than those identified, and (3) iodides with a larger than 3:1 stoichiometric ratio. More work will be required to understand what is happening.

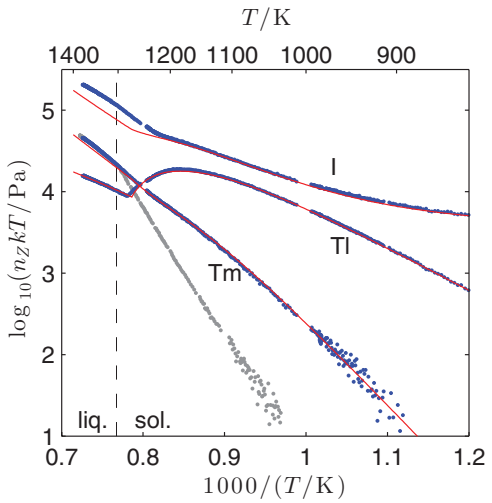

FIG. 15. Measured vapor pressures (blue) corresponding to the total vapor densities of Tm, Tl, and I in cell 8 nominally containing 8.8 mg of TmI_3 and 630 μg of TlI compared with calculations (red) for a cell containing 6.0 mg of TmI_3, 760 μg of TlI, and 4.2 μg of H_2O. Measurements of the vapor pressure corresponding to total density of Tm in cell 5 are shown in light gray.

VI. MEASUREMENT ERRORS AND UNCERTAINTIES

Statistical uncertainties associated with the noise particular to each individual spectral line and its immediate spectral region have been indicated by the error bars in the data figures. In this section, we discuss other sources of uncertainty and error.

The absolute scale of our measured values is determined using the calibration-by-substitution method with a nominally identical cell A3 containing a known pressure, and therefore number density, of Xe. The density of Xe in cell A3 was itself determined by fluorescence comparison with another cell whose density was measured with x-ray absorption to a precision of ±2%. This yielded a Xe density for A3 (see Table II) with a precision of ±11%. This is a systematic uncertainty that affects all of our measurements equally.

Systematic uncertainties, about which we know much less, are those due to errors in the atomic parameters such as photo-electric cross sections, branching fractions, and fluorescence yields. We estimate these to add less than 10% error combined, but that estimate is not rigorous.

The calibration procedure is affected randomly by the act of changing cells and by changes in temperature. This occurs because one of the limiting apertures for the fluorescence detection is the small hole in the side of the tantalum jacket. The detection efficiency is influenced by small changes in the position of this hole, relative to the slit assembly in front of the detector and relative to the x-ray beam, that occur when one cell is taken out and another put into the oven. It can also change when the oven temperature changes. To examine the magnitude of these effects, we first look at the four separate occasions when cell A3 was observed during our experiment at room temperature. These are shown in Figure 16. On each occasion, there were multiple consecutive measurements of the fluorescence intensity. Measurements from each

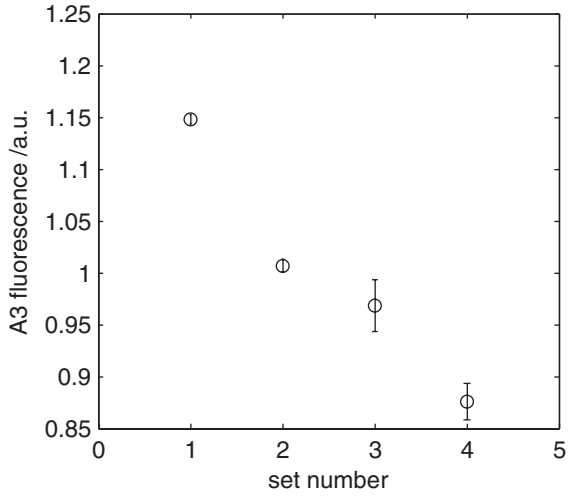

FIG. 16. Comparison of the Xe fluorescence intensity from cell A3 on four separate occasions, all at room temperature. The error bars represent the standard deviation of consecutive spectra within each set.

occasion have been averaged and the mean standard deviation of each set is reflected by the one-sigma error bars shown for each of the four occasions or sets. The latter are a couple percent or smaller, less than the differences between the mean values of each set, which span a total range of about 28%. Figure 17 shows the Xe fluorescence intensities on one occasion when we raised the oven temperature to more than 1300 K. The intensities show a mean variation of about 10% as the temperature rises. Expansion of the hole area over the same temperature interval is only about 1%. The error bars on the individual data points are attributable to the noise in the acquired spectra. (Each individual data point is based on fewer counts and therefore has a larger uncertainty than the points in Figure 16.) It is not clear that similar measurements on another cell would show the same variation with temperature, though the magnitude of the change could be expected to be comparable. It seems reasonable to attribute a combined uncertainty to these effects of ±20%. We treat this uncertainty as random.

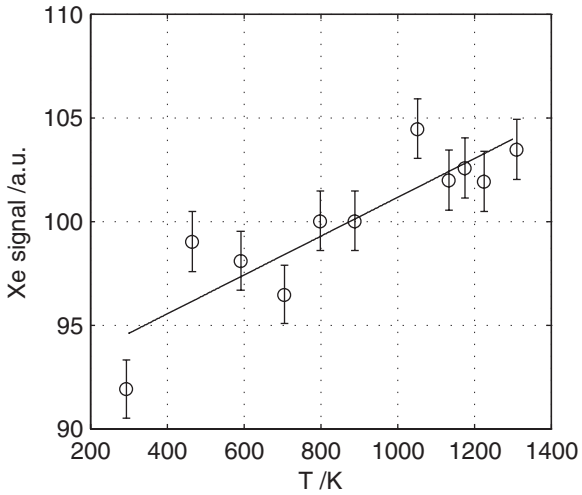

FIG. 17. Xe fluorescence intensity from cell B2 as a function of temperature.

The oven has an overall temperature time constant of approximately 25 min. This is sufficiently long that it is impractical to stabilize the oven temperature with a feedback loop while investigating a wide temperature range during a short period of time. Instead, we periodically increased the power to the oven and acquired data as the oven slowly came to equilibrium with the new power level. This procedure is valid as long as the cell comes to an equilibrium much more quickly than the oven is changing temperature. For cells 1, 3, 4, and 5, all of the measurements presented were acquired with the rate of temperature change no more than 0.067 K/s (4 K/min). Three-quarters of the data points were acquired with a temperature change of less than 0.034 K/s (2 K/min). The rate of temperature change during the observation of cell 8 was somewhat larger, as this cell was being examined as our allotted beam time was expiring. Figure 18 shows the measurements for Tm in cell 8 along with the time rate of change of the temperature as the temperature first increased (Tm in blue and dT/dt in cyan) and then decreased (Tm in green and dT/dt in magenta). The sawtooth shape of the time rate of change is produced by discrete changes in oven power. Immediately upon each increase in oven power, the time rate of change reached a local maximum, nearly 0.17 K/s (10 K/min) near $1000/(T/\mathrm{K}) = 0.8$. Here, small wiggles in the Tm data are visible, amounting to no more than 3% deviation of the vapor pressure from the longer term trend. Following each decrease in the oven power, the time rate of change reached a local minimum. There were 3 such decreases represented in the data here. During the first two, despite a time rate of temperature decrease of more than 0.08 K/s (5 K/min), the Tm measurements closely retraced the values obtained as the temperature increased. However, during the third decrease in power (the right-most green and magenta segments), the Tm vapor pressure values are about 5% less than the values obtained as the temperature increased. Although the corresponding time rate of temperature change is relatively small, the measurements were probably perturbed by the very large rate of temperature change which occurred just prior to the acquisition of these data points as the power to the oven was decreased. The temperature had been decreasing at a rate exceeding 2 K/s (120 K/min)! The rate of temperature change did not reach such magnitudes during the measurements presented in Figures 6–15. Errors from this source are likely no larger than 2% and are treated as random.

The transmitted flux showed some anomalous behavior (maximum 11%) at and above the melting temperature of the lanthanide salt for all cells. The reason for these anomalies is unknown, but it may indicate the movement of condensate onto or off of the windows through which the x-ray beam travels. Condensation on the downstream window does not affect the fluorescence measurement. Examination of the data during periods of anomalous transmission signals suggest that only during one episode did the effect on the measurements amount to as much as a few percent. Measurements of I in cell 1 just below the melting temperature of DyI_3 show a dip of about 10% that may be related these effects.

The uncertainty in vapor pressures due to random sources other than the spectral noise is estimated to be ±20%. The uncertainty of each data point, indicated by the error bars in the

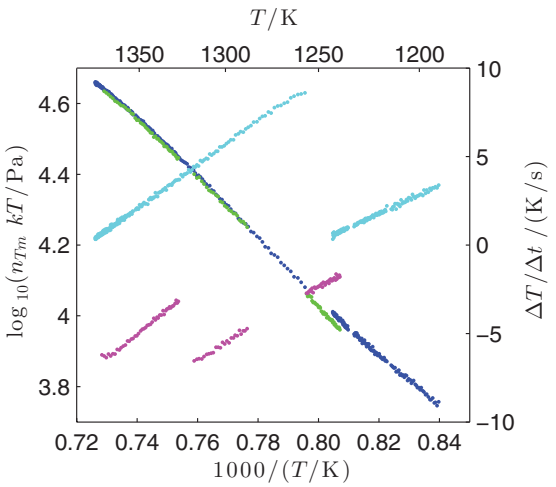

FIG. 18. An examination of the time rate of change of the cell temperature during measurements of cell 8. The points in dark blue and green show the vapor pressure corresponding to the total density of Tm while the temperature is increasing (dark blue) and decreasing (green). The magenta and cyan points give the time rate of change of temperature during the density measurements.

data figures, must be added in quadrature to this value in order to obtain the total uncertainty due to random sources. The total uncertainty in vapor pressures due to systematic effects is estimated to be ±23%.

Uncertainties in the temperature are also significant. The two ends of the tantalum jacket differed in temperature, presumably due to asymmetries in the custom-built oven. The difference was generally between 2 K and 4 K, with a handful of data points showing a 6 K to 8 K difference and a handful showing a 1 K difference. Averaging the two values probably eliminated most of this error, but the different values give some idea of the magnitude of temperature gradients. The center of the cell may well have been a few kelvin higher than the average of these temperatures. At the same time, the cold spot in the cell, where the condensate was established, may well have been a few kelvin cooler. We have not tried to correct for either of these effects. We estimate that our temperature uncertainty from this source is ±5 K. Most spectra were integrated for 30 s or less. This lead to temperature changes during each acquisition that were generally less than 2 K, but sometimes nearly 3 K. We averaged the initial and final temperatures. We estimate our temperature uncertainty from this affect as ±1 K. The type-N calibrated thermocouples are believed to be accurate to ±1 K. We estimate our overall temperature uncertainty to be ±5 K.

We also note that visual inspection of the cells after measurements did not show any indication of reaction of the salts with the walls of the vapor cells.

As discussed in the preceding section, salt doses in the cells probably differed from their nominal values. Variations in a minority salt make a difference in the performance of the system. This does not affect the accuracy of our measurements, but it does add uncertainty about what system we are measuring.

VII. CONCLUSION

X-ray induced fluorescence and thermochemical equilibrium simulations have been used to understand aspects of the vapors in equilibrium with DyI_3, DyI_3/InI, TmI_3, and TmI_3/TlI condensates. Absolute measurements of the vapor pressures corresponding to the total densities of each element were obtained in closed systems for temperatures ranging from 900 K to 1400 K.

In the mixed salt systems, the amount of lanthanide in the vapor was strongly enhanced by the presence of the second metal-iodide salt. The enhancements were explained in terms of hetero-complexes in the vapors and the liquid condensates. The enhancement of the lanthanide in both systems is confined to temperatures lower than the melting temperature of the pure lanthanide salt. Some aspects of iodine behavior were not explained by the modeling.

Vapor-phase complexing in the systems studied here is primarily effective at temperatures below the steady-state cold-spot temperatures in most commercial metal-halide HID lamps. The enhancement of the lanthanide in the vapor phase might be useful for decreasing the apparent warm-up time of metal-halide lamps, when lamp output is inefficient and of poor color.

ACKNOWLEDGMENTS

We thank Steve Hansen of Anderson Physical Labs for helpful suggestions; the management of OSRAM SYLVANIA for supporting this project; our OSRAM SYLVANIA colleagues Joanne Browne, Victor Perez, Jeff Neil, Michael Quilici, and John Kelso for their expert technical assistance; Ali Mashayekhi and Roger Ranay of the Advanced Photon Source for their help on the beamline. Use of the Advanced Photon Source was supported by the U. S. Department of Energy, Office of Science, Office of Basic Energy Sciences, under Contract No. DE-AC02-06CH11357.

[1]G. G. Lister, J. E. Lawler, W. P. Lapatovich, and V. A. Godyak, Rev. Mod. Phys. **76**, 541 (2004).
[2]R. Lorenz, Light. Res. Technol. **8**, 136 (1976).
[3]C. Hirayama, P. M. Castle, C. S. Liu, and R. J. Zollweg, J. Illum. Eng. Soc. **6**, 209 (1977).
[4]K. Hilpert, J. Electrochem. Soc. **136**, 2099 (1989).
[5]S. Boghosian and G. N. Papatheodorou, in *Handbook on the Physics and Chemistry of Rare-Earths*, edited by K. A. Gschneidner, Jr. and L. Eyring (Elsevier Science, Amsterdam, 1996), Vol. 23, Chap. 157, p. 435.
[6]J. W. Hastie, *High Temperature Vapors* (Academic Press, New York, 1975).
[7]J. J. Curry, E. G. Estupiñán, A. Henins, W. P. Lapatovich, and S. D. Shastri, Chem. Phys. Lett. **507**, 52 (2011).
[8]J. J. Curry, E. G. Estupiñán, A. Henins, W. P. Lapatovich, S. D. Shastri, and J. E. Hardis, Appl. Phys. Lett. **100**, 083505 (2012).
[9]J. J. Curry, W. P. Lapatovich, and A. Henins, in *Advances in Atomic, Molecular, and Optical Physics*, edited by E. Arimondo, P. Berman, and C. C. Lin (Academic Press, San Diego, 2011), Vol. 60, Chap. 2.
[10]N. A. Dyson, *X-rays in Atomic and Nuclear Physics*, 2nd ed. (Cambridge University Press, Cambridge, 1990), Chap. 3.
[11]S. D. Shastri, K. Fezzaa, A. Mashayekhi, W.-K. Lee, P. B. Fernandez, and P. L. Lee, J. Synchrotron Radiat. **9**, 317 (2002).
[12]M. J. Berger, J. H. Hubbell, S. M. Seltzer, J. Chang, J. S. Coursey, R. Sukumar, D. S. Zucker, and K. Olsen, *Xcom: Photon cross sections database, NIST standard reference database 8*, see http://www.nist.gov/pml/data/xcom/index.cfm (1998).
[13]M. O. Krause, J. Phys. Chem. Ref. Data **8**, 307 (1979).

[14]P. V. Rao, M. H. Chen, and B. Crasemann, Phys. Rev. A **5**, 997 (1972).
[15]D. R. Cruise, J. Phys. Chem. **68**, 3797 (1964).
[16]*NIST-JANAF Thermochemical Tables*, 4th ed., edited by J. M. W. Chase (American Chemical Society/American Institute of Physics, Woodbury, NY, 1998).
[17]*Thermochemical Data of Pure Substances*, 2nd ed., edited by I. Barin (in collaboration with F. Sauert, E. Schultze-Rhonhof, and W. S. Sheng) (Verlagsgesellschaft mbH, New York, 1993).
[18]See supplementary material at http://dx.doi.org/10.1063/1.4821828 for text file of measured pressure values.
[19]D. Kobertz, K. Hilpert, and S. Hansen, in *Proceedings of the 12th International Symposium on the Science and Technology of Light Sources and the 3rd International Conference on White LEDs and Solid State Lighting, Eindhoven, The Netherlands*, edited by M. Haverlag, G. M. W. Kroesen, and T. Taguchi (FAST-LS Ltd., UK, 2010), p. 521.
[20]K. Hilpert, M. Miller, and F. Ramondo, Thermoch. Acta **417**, 163 (2004).
[21]O. Kaposi, L. Lelik, and K. Balthazár, High. Temp. Sci. **16**, 311 (1983).
[22]M. Ohnesorge, Ph.D. thesis, Forschungszentrum Jülich, 2005).
[23]S. Hansen, R. Steward, J. Getchius, and T. Brumleve, *Supplement To Vapor Pressure of Metal Bromides and Iodides* (APL Engineered Materials, Inc., Urbana, IL, 2000).
[24]B. H. Mahan, *University Chemistry*, 3rd ed. (Addison-Wesley, 1975).
[25]J. H. Dettingmeijer and H. R. Dielis, J. Less-Common Met. **139**, 331 (1988).
[26]T. Karwath, D. Kobertz, and K. Hilpert, in *Molten Salt Chemistry and Technology*, edited by H. Wendt (Trans Tech Publication Ltd., Switzerland, 1998), Vol. 5, p. 223.